Journal of Alloys and Compounds 521 (2012) 150–154

Contents lists available at SciVerse ScienceDirect

Journal of Alloys and Compounds

journal homepage: www.elsevier.com/locate/jallcom

Synthesis and dielectric properties of textured $SrBi_2Nb_2O_9$ ceramics via laser rapid solidification

Junji Zhang, Mingju Chao*, Erjun Liang, Mingyu Li

Key Laboratory of Materials Physics of Ministry of Education of China, School of Physical Science and Engineering, Zhengzhou University, Zhengzhou 450052, China

ARTICLE INFO

Article history:
Received 11 November 2011
Received in revised form 10 January 2012
Accepted 16 January 2012
Available online 28 January 2012

Keywords:
Laser rapid solidification
$SrBi_2Nb_2O_9$
Texture
Dielectric property

ABSTRACT

Textured poly-crystalline $SrBi_2Nb_2O_9$ (SBN) with a preferred ⟨0 1 0⟩ orientation ceramics were synthesized via laser rapid solidification using a CO_2 laser. X-ray diffraction analysis reveals that the preferred orientation of the as-obtained SBN is along the *b*-axis, and the orientation factor is approximately 0.78. Scanning electron microscope image shows that the as-obtained SBN is composed of flake-like grains with maximum thickness and length of 1.0 μm and 0.1 mm, respectively, which are parallel to the laser incident direction. The directional solidification produces the textured structure, and the shortest *b*-axis length determines that the preferred orientation direction is along the *b*-axis. Dielectric property research demonstrates that the phase transition of the as-obtained SBN is diffuse, which may be due to the orientation array of the grains.

1. Introduction

Bismuth layer-structured ferroelectrics (BLSFs) have attracted much attention due to their potential application in ferroelectric non-volatile random access memory [1–7]. The BLSFs are composed of layers of pseudo-perovskite blocks $(A_{n-1}B_nO_{3n+1})^{2-}$ interleaved with bismuth oxide $(Bi_2O_2)^{2+}$ layers along the pseudo-tetragonal *c*-axis. Due to the particular layer structure, BLSFs possess distinct anisotropy between the *a*(*b*)-axis (*a*–*b* plane) and *c*-axis directions [8,9]. In order to improve the ferroelectric property which is mainly affected by the orientation of the grains, several textured BLSFs ceramics were synthesized by various routes, such as hot-forging [9], spark plasma sintering [10], melt-quenching [11], template grain growth [12–14], and reactive template grain growth [15] methods. The preferred orientation of the BLSFs ceramics obtained via mentioned methods is usually along the *c*-axis (⟨0 0 1⟩ plane). In addition, these methods are complex, time-consuming, and may bring pollution to sample in the synthesis process. So it is necessary to find a new method to synthesize textured BLSFs ceramics with a preferred ⟨0 1 0⟩ orientation.

High-power lasers are widely used in industries as well as in laboratories for cladding [16,17], cutting [18], thin film deposition via laser ablation [19,20] and so on. Recent research found that pure bulk ceramic materials could also be synthesized through rapid solidification using a high power laser as the heat source [21–24]. This route is named as laser rapid solidification (LRS). Compared with commonly used routes, LRS is a novel and rapid method that can produce tens of grams of a sample in a few minutes, and can reduce the probability of pollution to a sample. In our previous work, textured $BaTi_2O_5$ with a preferred ⟨0 1 0⟩ orientation was fabricated by LRS method and the generation of orientated grains was attributed to its natural characteristics [24]. In this article, $SrBi_2Nb_2O$ (one of the BLSFs ceramics with $n = 2$, SBN) with a preferred orientation along ⟨0 1 0⟩ plane was fabricated through LRS route, and the textured microstructure was analyzed from the angle of grain growth. The dielectric properties in this preferred direction was also studied.

2. Experimental details

Reagent grade $SrCO_3$ (99.0%), Bi_2O_3 (99.0%), and Nb_2O_5 (99.5%) used as the starting materials in the current study were dried at 150 °C for 2 h in a baking oven before weighting. The amounts of raw materials were mixed according to the stoichiometric ratios of SBN. Different additional contents of Bi_2O_3 (10, 20, 30, 40, 50, 60, and 70 wt.%) were supplemented to the initial mixture to compensate for the bismuth loss in the LRS process. The mixtures were ground in an agate mortar for 2 h using a pestle and pressed into a cylinder with a diameter of 13 mm and a thickness of 4 mm using a uni-axial cold press in a steel mold at a pressure of 20 MPa. The weight of each pressed sample was approximately 4 g.

The LRS synthesis method was performed using a continuous-wave CO_2 laser (TJ-HL-5000). The sample was placed on a horizontal tabulate stainless steel test bed. The laser beam was striking vertically onto the sample's surface at a distance where the defocus length was set to 120 mm and the beam spot was approximately 13 mm in diameter. The power of the output laser was set to 600 W. Subsequently, the laser beam was opened to sinter the front face for 50 s, the beam was closed, and the sample was reversed to repeat all the processes for the other face (30 s sintering time). When the laser beam was closed, a stainless steel plate was placed on the melt sample and stained its surface parallel to the test bed in the solidification processing.

* Corresponding author. Tel.: +86 371 67767836; fax: +86 371 67766629.
E-mail address: chaomingju@zzu.edu.cn (M. Chao).

0925-8388/$ – see front matter © 2012 Elsevier B.V. All rights reserved.
doi:10.1016/j.jallcom.2012.01.099

In this processing, all the samples completely melted into globular liquid droplets and then solidified into plate-like bulks in a few minutes. In the phase analysis and electrical characterization, as-obtained bulks were manually sanded to thin disks with about 1.5 mm in thickness using sand paper. The sanding direction was parallel to the interface of the bulk and the test bed. For comparison, SBN ceramics prepared via the conventional mixed oxide method were sintered at 1200 °C for 2 h using an electrical furnace.

The laser rapid solidification synthesis route was performed by a continuous-wave CO_2 laser (TJ-HL-5000). The density of samples was measured by the Archimedes method. The phase analysis of the BT2-LRS samples was carried out using an X'Pert PRO X-ray diffractometer at room temperature. The degree of orientation (f) was calculated by Lotgering's method. The cross-section microstructures were observed with a JSM-6700F scanning electron microscope. Platinum paste was painted on opposite of the thin disks and sintered at 1000 °C for 30 min as the electrodes. The dielectric constants were carried out using a HP 4294A precision impedance analyzer as a function of temperature (room temperature to 490 °C) and frequency (10 kHz to 1 MHz) in air.

3. Results and discussion

3.1. X-ray diffraction analysis

The bulk and powder XRD pattern of the SBN ceramic synthesized via the conventional solid-state reaction-sintering route (denoted as SBN-SRS) is shown in Fig. 1. All the diffraction peaks of the powder XRD pattern are well consistent with JCPDS (49-0607). This result indicates that the SBN-SRS sample is in a highly pure orthorhombic phase. In the LRS processing, the power of the laser beam was approximately 600 W and the temperature of the sintered samples was over 1500 °C, which is evidently higher than the melting point of Bi_2O_3 (approximately 820 °C). Considering the high volatility of bismuth at high temperatures, extra Bi_2O_3 (x = 10, 20, 40, 50, 60, and 70 wt.%) was added into the mixtures to compensate for bismuth loss. In addition, to get a series of comparable results, all experimental parameters, including sintering time, laser power, and defocus length, remained unchanged for the LRS of the samples with different Bi_2O_3 contents. The bulk XRD pattern of the SBN ceramic synthesized via the LRS method with different initial Bi_2O_3 content mixtures (SBNx-LRS) are shown in Fig. 1a. In order to further study the possible impurity phase which may be generated due to the bismuth volatilization during the LRS process [25], powder XRD pattern of the SBN-LRS and SBN-SRS was also measured and shown in Fig. 1b.

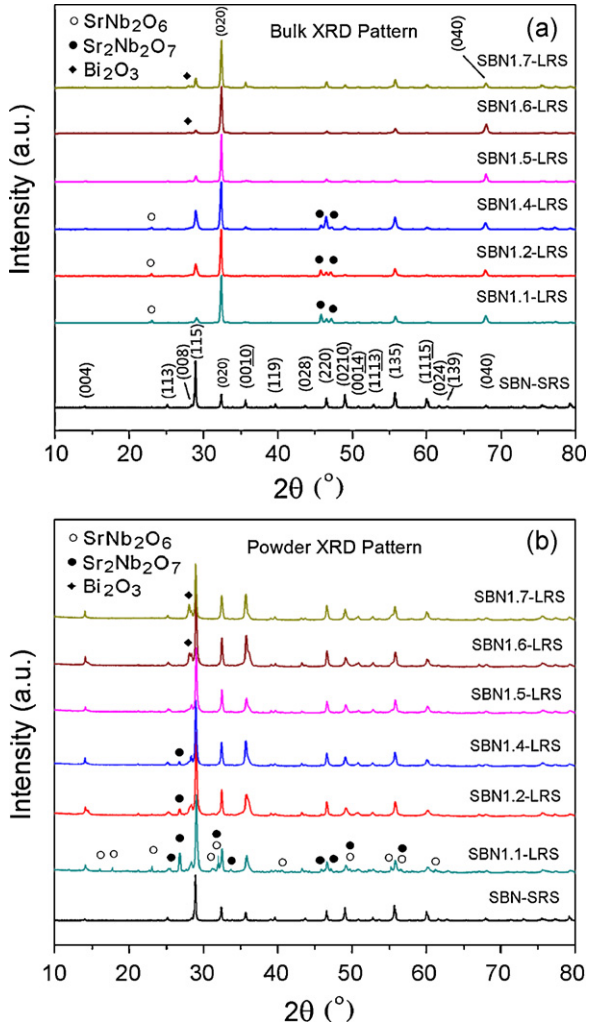

Fig. 1. (a) Bulk and (b) powder XRD patterns of SBN-SRS and SBNx-LRS.

As shown in Fig. 1, a few reflections corresponding to $SrNb_2O_6$ (28-1243) and $Sr_2Nb_2O_7$ (72-0704) were found in the patterns of SBN1.1-LRS, SBN1.2-LRS and SBN1.4-LRS. The additional 10–40 wt.% Bi_2O_3 content may not be enough to compensate for the loss and several impurities present during the sintering process. However, in the patterns of the samples with extra 60 and 70 wt.% Bi_2O_3 contents (SBN1.6-LRS and SBN1.7-LRS), a few reflections corresponding to Bi_2O_3 were also found. This result implies that the additional 60 and 70 wt.% Bi_2O_3 contents were excessive. In the XRD pattern of the sample with extra 50 wt.% Bi_2O_3 content (SBN1.5-LRS), no impurity phase, such as $SrNb_2O_6$, $Sr_2Nb_2O_7$, or Bi_2O_3, was observed. This result indicates that 1:1.5:1 ($SrCO_3$:Bi_2O_3:Nb_2O_5, mole rate) is the optimum ratio of the starting materials in that given experimental parameter. In addition, pure ceramics with highly volatile elements can be also synthesized successfully through this method by properly adding extra contents of corresponding raw materials (Bi_2O_3, in the present SBN sample) into the starting charge mixture.

In the laser sintering process, the chemical reaction can be processed efficiently because the mixtures melted into droplet-like molten pool in which strong thermal and matter convection existed. Furthermore, this method promotes the generation of highly pure orthorhombic SBN in tens of seconds. For SBNx-LRS sample, significant difference is observed in the intensity of the diffraction peak between disk and powder XRD pattern, although the 2θ value of the diffraction peak are well consistent. For the non-textured SBN-SRS disk or SBNx-LRS powder, the strongest diffraction peak is (1 1 5), which is consistent with the (1 1 ($2n$ + 1)) highest diffraction peak in the Aurivillius phase [26]. However, the most intense peak for SBN-LRS is (0 2 0), which is just a medium peak for SBN-SRS or SBNx-LRS powder. In addition, the medium intense (0 4 0) peak for SBN-LRS is just a weak peak for SBN-SRS or SBNx-LRS powder. The relative intensities (0 2 0) and (0 4 0) are evidently much higher than that of the non-textured SBN-LRS or SBNx-LRS. The orientation of the grains is along the ⟨0 1 0⟩ plane, and the tangential direction of the ⟨0 1 0⟩ plane is parallel to the surface of the samples. In other words, the orientation of the grains is along the b-axis direction perpendicular to the surface of the samples. The sample with the highest purity (x = 50 wt.%, SBN1.5-LRS, denoted as SBN-LRS in the following) is selected to be studied in the following text.

The degree of orientation (Lotgering's factors, f) of SBN-LRS was calculated using the following Lotgering's method:

$$f = \frac{(P - P_0)}{(1 - P_0)}, \quad P = \frac{\sum I_{\{0\,k\,0\}}}{\sum I_{\{h\,k\,l\}}}, \quad P_0 = \frac{\sum I_{0\{0\,k\,0\}}}{\sum I_{0\{h\,k\,l\}}} \tag{1}$$

where I and I_0 are the peak intensities of the sintered compact and randomly oriented SBN, respectively, and $\{0\,k\,0\}$ and $\{h\,k\,l\}$ are Miller indices. The diffraction lines between $2\theta = 10°$ and $2\theta = 80°$ were used to calculate P and P_0. The f value of the ⟨0 1 0⟩ orientation

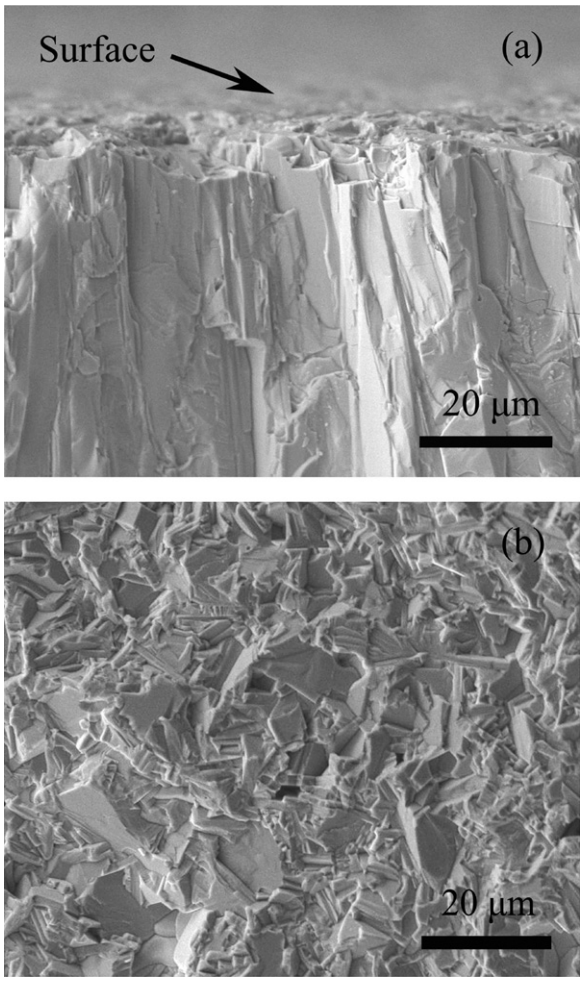

Fig. 2. Cross-section SEM of (a) SBN-LRS and (b) SBN-SRS ceramic.

was calculated to be 0.78 using Eq. (1). This result demonstrates that SBN-LRS ceramic is with a relatively high degree of *b*-axis orientation.

3.2. Microstructures and grains growth analysis

The grain alignments were also evaluated by observing the SEM images. Fig. 2 shows typical cross-section SEM images of the SBN sample synthesized via LRS and SRS. As shown in Fig. 2a, SBN-LRS is composed of well-developed, compact flake-like grains and that its plate-like grains grow gradually with obvious orientated growth tendency in the cross-section with little pores. Thus, SBN-LRS has a high density of 7.23 g/cm^3. The well-developed flakes are evidently perpendicular to the surface of the sample and approximately parallel to the laser incident direction. The maximum thickness and length of the flake-like SBN grains are 1 μm and 0.1 mm, respectively. The SEM image of SBN-SRS (Fig. 2b) shows that the grains of SBN-SRS are randomly arrayed with an even size and a few pores. This result is also consistent with its relatively low density of 7.06 g/cm^3. The differences in the grain arrangement between the above two samples are consistent with the differences in their XRD patterns. The SEM observation illustrates the fact that the SBN-LRS is texture-orientated from another angle.

The relative growth ratio of different planes is inversely proportional to the point density of lattice planes [27,28]. The crystallographic parameters of SBN can be searched from PDF 49-0607, $a = 0.55239$ nm, $b = 0.55136$ nm, $c = 2.51208$ nm, and $\alpha = \beta = \gamma = 90^\circ$. Among the three axes, the length of the *b*-axis length is the shortest. Thus, the ⟨0 1 0⟩ plane has the lowest point density (0.7206 points per square nanometer) and the lowest interplanar spacing (0.55136 nm, *b*-axis length) compared with the ⟨0 0 1⟩ and ⟨1 0 0⟩ planes. Consequently, the ⟨0 1 0⟩ plane has the highest growth ratio during the growth of the SBN grains in the solidification process. The growth direction of the grains is same as the temperature gradient direction, which is perpendicular to the surface and pointing to interior of the sample. Therefore, the grains will generate first in the interface of the sample and test bed, and then grow gradually in the sample interior with a preferred growth direction along the *b*-axis. After the solidification is completed, the obtained bulk sample shows a textured microstructure with the ⟨0 1 0⟩ plane parallel to its surface, which explains the intense (0 2 0) and (0 4 0) diffraction peaks of SBN-LRS shown in Fig. 1. In conclusion, the textured structure resulted from directional solidification, and the axis length of the unit cell along the shortest axis direction determines the preferred orientation direction. This conclusion is also appropriate to explain the preferred orientation of textured $BaTi_2O_5$ synthesized by LRS route [24], where the *b*-axis of $BaTi_2O_5$ is also with a shortest length and the generation of preferred grains was simply attributed to its natural characteristics of growth along *b*-axis. Based on the characteristics of efficient chemical reaction and rapid directional solidification of LRS route, more textured ceramics with preferred orientation along the shortest axis length direction may be fabricated by properly increasing the content of volatile raw materials if the aimed compounds contain volatile elements.

3.3. Dielectric properties analysis

The dielectric properties of the SBN-LRS and SBN-SRS are also studied. Fig. 3 shows the temperature dependence of the dielectric constant ε and loss $\tan\delta$ measured at several frequencies for the SBN-LRS and SBN-SRS sample. Fig. 3a illustrates that all the curves obtained at the different measured frequencies show broader dielectric peaks, and all the temperature T_m corresponding to the temperature of the dielectric constant maximum is 317.4 °C. The dielectric loss $\tan\delta$ shown in Fig. 3b maintains a low value and increases with temperature when the temperature is higher than 170 °C. At room temperature (27 °C), ε is approximately 180 with a low loss $\tan\delta$ of 0.0218 at 10^5 Hz. The dielectric peak of a normal ferroelectric ceramic is always very sharp and its T_m value hardly varies with the probed frequency. Fig. 3c shows that the dielectric peak of SBN-LRS is very sharp and the T_m values are 439 °C consistently. These illustrate that SBN-LRS is a normal ferroelectric and consistent with the literatures [29,30]. However, compared to the T_m value of SBN-SRS, the value for SBN-LRS is lower, about 121.6 °C. The reason for the diminution of T_m may be attributed to the ⟨0 1 0⟩ plane preferred orientation microstructure tentatively and it should be studied further in the future. The broad dielectric peaks present at each measured frequency imply that the SBN-LRS probably is a diffuse transition ferroelectric, although the T_m values of different probed frequencies are the same. To evaluate the diffuse behavior for SBN-LRS, several quantitative characterizations were conducted.

The dielectric constant ε of a normal ferroelectric, above the Curie temperature follows the Curie–Weiss law described by

$$\varepsilon^{-1} = C^{-1} \times (T - T_0) \quad (T > T_0) \tag{2}$$

where *C* is the Curie–Weiss constant and T_0 is the Curie–Weiss temperature. The inverse dielectric constant $(1/\varepsilon)$ as a function of temperature at 10^5 Hz for SBN-LRS and SBN-SRS ceramic is plotted in Fig. 4. The experimental data were fitted by Eq. (2) using a fitting program, and the fitting parameters T_0 and *C* are 122.9 and 1.99×10^5 °C for SBN-LRS, and 389.9 and 4.05×10^4 °C for SBN-SRS, respectively. The parameter ΔT_m illustrates the degree of the

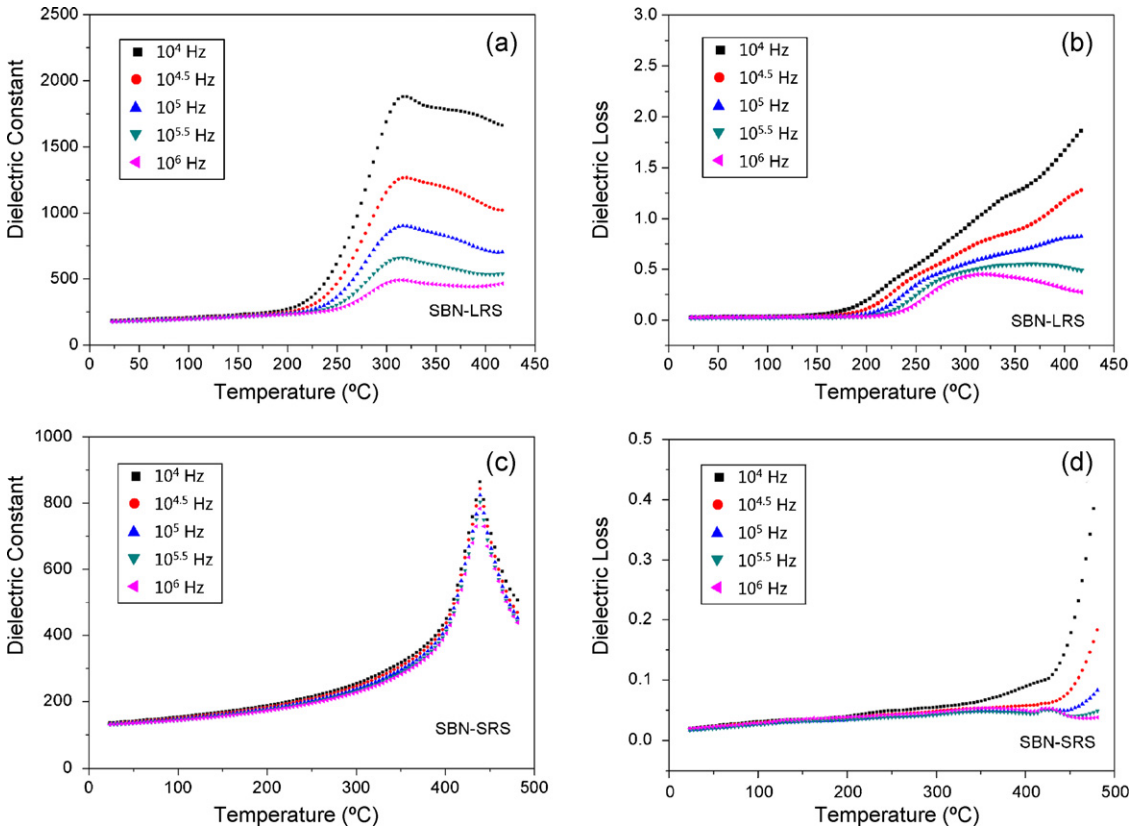

Fig. 3. Dielectric constant ε and loss tan δ as a function of temperature: (a) and (b) for SBN-LRS, and (c) and (d) for SBN-SRS, measured at different frequencies (10^4, $10^{4.5}$, 10^5, $10^{5.5}$ and 10^6 Hz).

deviation from the Curie–Weiss law and is defined as the following [31,32]:

$$\Delta T_m = T_{CW} - T_m \tag{3}$$

where T_{CW} is the temperature at which dielectric constant ε starts to follow the Curie–Weiss law, and T_m is the temperature at which the ε value reaches the maximum. The parameters T_{CW}, T_m, and ΔT_m are 370.9, 317.4, and 53.5 °C for SBN-LRS, and 440, 439 and 1 °C for SBN-SRS, respectively. The ΔT_m value for SBN-LRS is larger than that of a normal ferroelectric whose value is usually about 0. The larger ΔT_m value indicates a diffusive phase transition for SBN-LRS and corresponds to the broad dielectric peak shown in Fig. 4a.

To further evaluate the diffusion of phase transition, a modified empirical expression proposed by Uchino and Nomra [33] was employed in the present work:

$$\varepsilon^{-1} - \varepsilon_m^{-1} = C_1^{-1} \times (T - T_m)^{\gamma} \tag{4}$$

where ε_m is the maximum value of the electric constant at the transition temperature (T_m), C_1 is the Curie-like constant, γ is the diffuseness of the transition and its value is between 1 and 2. The parameter γ gives information on the characteristics of the

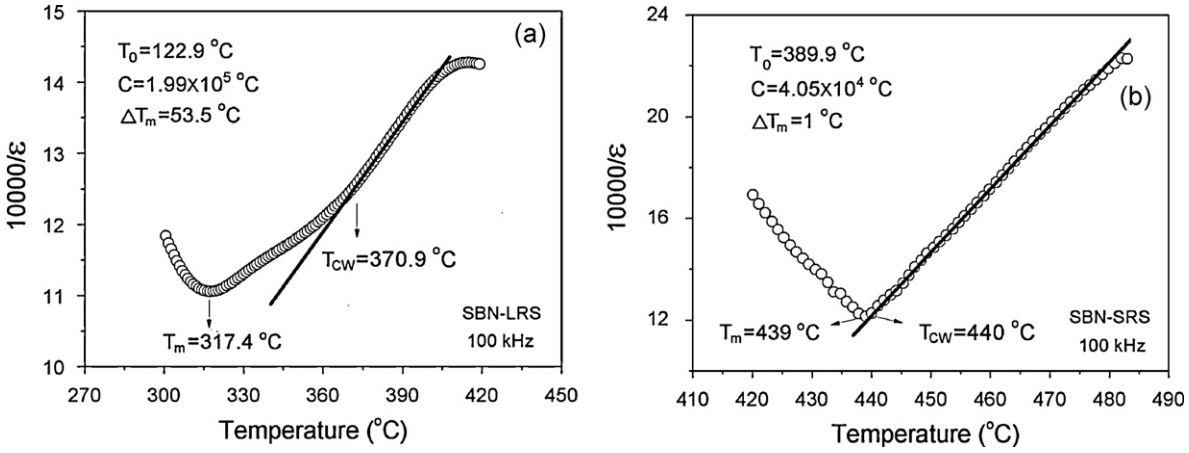

Fig. 4. The inverse dielectric constant ($1/\varepsilon$) as a function of temperature at 10^5 Hz: (a) for SBN-LRS and (b) for SBN-SRS ceramic (symbol: experimental data; solid line: fitting to Eq. (2)).

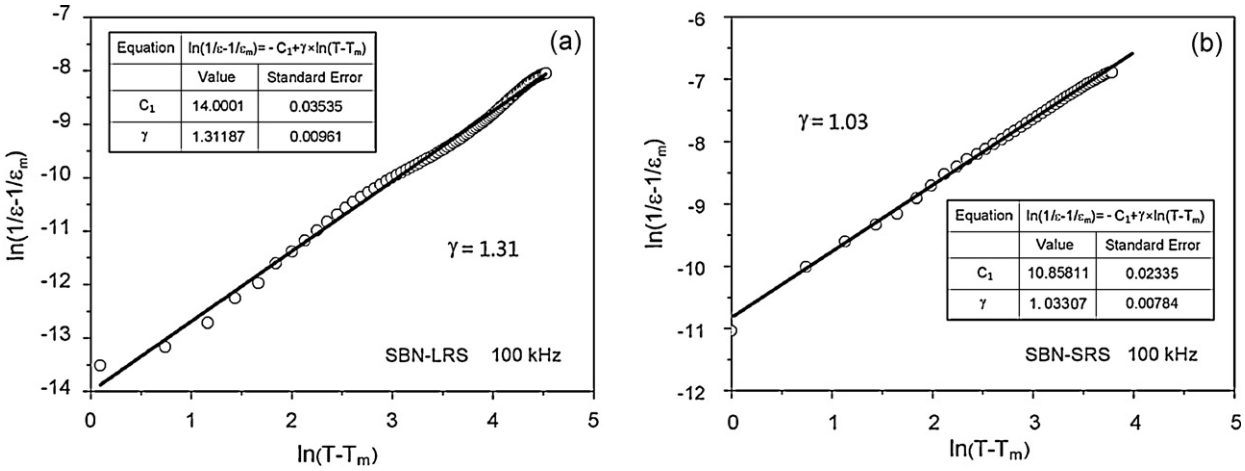

Fig. 5. Plot of $\ln(1/\varepsilon - 1/\varepsilon_m)$ as a function of $\ln(T - T_m)$ at 10^5 Hz: (a) for SBN-LRS and (b) for SBN-SRS ceramic (symbol: experimental data; solid line: fitting to Eq. (4)).

phase transition. The limiting values $\gamma = 1$ and $\gamma = 2$ obeying the Curie–Weiss law are the characteristics of a normal ferroelectric and an ideal relaxor ferroelectric, respectively. Fig. 5 shows the plot of $\ln(\varepsilon^{-1} - \varepsilon_m^{-1})$ as a function of $\ln(T - T_m)$ for SBN-LRS and SBN-SRS ceramics measured at 10^5 Hz. A linear fitting method was adopted to calculate the value of γ based on Eq. (4). As shown in Fig. 5, the γ value for SBN-LRS is approximately 1.31, which is determined by the slope of the fitting line. The γ value is higher than that of SBN (about 1.03) obtained via the SRS method.

The broader dielectric peak, as well as the larger ΔT_m and γ values of the SBN-LRS, demonstrates that the SBN-LRS is a diffuse transition ferroelectric material. The diffuseness of the transition may be due to the ordering of the dipoles rendered by the textured structure [11]. More and detailed properties of the SBN-LRS will be reported soon.

4. Conclusions

Textured SBN ceramic oriented along the *b*-axis was synthesized via the LRS method using a CO_2 laser. The addition of the different extra Bi_2O_3 contents into the starting materials is necessary to compensate for the Bi loss in the LRS process and contribute to obtain a pure poly-crystal SBN. The high temperature and the strong thermal and matter convection of the LRS method promote efficient generation of SBN. The directional temperature gradient, solidification direction, and the shortest *b*-axis length of its unit cell together prove that the grains grow preferentially in the *b*-axis direction, and that the plate-like microstructure form ultimately. The ordering of the dipoles may result in the diffuseness of the transition for SBN-LRS. As a simple, fast, and efficient method, LRS can be extended for the synthesis of more textured ceramic materials.

Acknowledgements

This work is supported by the National Natural Science Foundation of China (Grant No. 51072238) and the Technologies R&D Program of Zhengzhou City (Grant No. 112PPTGY219-9).

References

[1] C. Dearaujo, J.D. Cuchiaro, L.D. Mcmillan, M.C. Scott, J.F. Scott, Nature 374 (1995) 627.
[2] B.H. Park, B.S. Kang, S.D. Bu, T.W. Noh, J. Lee, W. Jo, Nature 401 (1999) 682–684.
[3] D. Kajewski, Z. Ujma, J. Alloys Compd. 509 (2011) 7532–7536.
[4] R. Sridarane, S. Subramanian, N. Janani, R. Murugan, J. Alloys Compd. 492 (2010) 642–648.
[5] K. Miura, Appl. Phys. Lett. 80 (2002) 2967–2969.
[6] Z.H. Peng, Q. Chen, J.G. Wu, X.H. Zhu, D.Q. Xiao, J.G. Zhou, J. Alloys Compd. 509 (2011) 8483–8486.
[7] P.Y. Fang, H.Q. Fan, L.J. Liu, J. Chen, J. Li, J. Alloys Compd. 477 (2009) 828–831.
[8] Z. Li, H.L.W. Chan, Y. Li, K.W. Kwok, S.H. Choy, J. Alloys Compd. 506 (2010) 70–72.
[9] H. Ogawa, A. Kan, Y. Nakamura, J. Alloys Compd. 473 (2009) 567–570.
[10] H.X. Yan, H.T. Zhang, R. Ubic, M. Reece, J. Liu, Z.J. Shen, J. Mater. Sci. Mater. Electron. 17 (2006) 657–661.
[11] K. Majhi, B.R. Varma, J. Electroceram. 25 (2010) 70–76.
[12] M. Kimura, H. Ogawa, T. Sawada, K. Shiratsuyu, N. Wada, A. Ando, J. Electroceram. 21 (2008) 55–60.
[13] J.A. Horn, S.C. Zhang, U. Selvaraj, G.L. Messing, S. Trolier-McKinstry, J. Am. Ceram. Soc. 82 (1999) 921–926.
[14] H. Amorín, A.L. Kholkin, M.E.V. Costa, J. Eur. Ceram. Soc. 25 (2005) 2453–2456.
[15] T. Takeuchi, T. Tani, Y. Saito, Jpn. J. Appl. Phys. Part 1 38 (1999) 5553–5556.
[16] S.F. Zhou, X.Y. Zeng, J. Alloys Compd. 505 (2010) 685–691.
[17] M.J. Chao, W.L. Wang, E.J. Liang, D.X. Ouyang, Surf. Coat. Technol. 202 (2008) 1918–1922.
[18] A. Riveiro, F. Quintero, F. Lusquinos, R. Comesana, J. Pou, Appl. Surf. Sci. 257 (2011) 5393–5397.
[19] J.J. Wang, C.B. Wang, Q. Shen, L.M. Zhang, J. Alloys Compd. 512 (2012) 140–143.
[20] P.X. Yang, D.L. Carroll, J. Ballato, R.W. Schwartz, J. Appl. Phys. 93 (2003) 9226–9230.
[21] E.J. Liang, T.A. Wu, B. Yuan, M.J. Chao, W.F. Zhang, J. Phys. D: Appl. Phys. 40 (2007) 3219–3223.
[22] E.J. Liang, J.P. Wang, E.M. Xu, Z.Y. Du, M.J. Chao, J. Raman Spectrosc. 39 (2008) 887–892.
[23] J. Zhang, E.J. Liang, X.H. Zhang, J. Power Sources 195 (2010) 6758–6763.
[24] J.J. Zhang, J.M. Yu, M.J. Chao, E.J. Liang, M.Y. Li, D.C. Li, J. Mater. Sci. 47 (2012) 1554–1558.
[25] M. Peiteado, M.A. de la Rubia, M.J. Velasco, F.J. Valle, A.C. Caballero, J. Eur. Ceram. Soc. 25 (2005) 1675–1680.
[26] X.F. Du, I.W. Chen, J. Am. Ceram. Soc. 81 (1998) 3253–3259.
[27] A.S. Myerson, Molecular Modeling Applications in Crystallization, Cambridge University Press, Cambridge, 1999, pp. 102–104.
[28] C. Suryanarayana, Non-Equilibrium Processing Of Materials, Pergamon Press, Oxford, 1999, pp. 278–282.
[29] L. Sun, C. Feng, L. Chen, S. Huang, J. Am. Ceram. Soc. 90 (2007) 322–326.
[30] S. Huang, Y. Li, C. Feng, M. Gu, X. Liu, J. Am. Ceram. Soc. 91 (2008) 2933–2937.
[31] X.G. Tang, X.X. Wang, K.H. Chew, H.L.W. Chan, Solid State Commun. 136 (2005) 89–93.
[32] J. Hao, Z. Xu, R. Chu, W. Li, G. Li, Q. Yin, J. Alloys Compd. 484 (2009) 233–238.
[33] K. Uchino, S. Nomura, Ferroelectr. Lett. Sect. 44 (1982) 55–61.